Magnetocrystalline anisotropy of the easy-plane metallic antiferromagnet Fe_2As

Kexin Yang,[1,2] Kisung Kang,[2,3] Zhu Diao,[2,4,5,†] Manohar H. Karigerasi,[2,3] Daniel P. Shoemaker,[2,3] André Schleife,[2,3,6] and David G. Cahill[1,2,3,*]

[1]*Department of Physics, University of Illinois at Urbana-Champaign, Urbana, Illinois 61801, USA*
[2]*Materials Research Laboratory, University of Illinois at Urbana-Champaign, Urbana, Illinois 61801, USA*
[3]*Materials Science and Engineering, University of Illinois at Urbana-Champaign, Urbana, Illinois 61801, USA*
[4]*Department of Physics, AlbaNova University Center, Stockholm University, SE-106 91 Stockholm, Sweden*
[5]*Department of Physics, Florida A&M University, Tallahassee, Florida 32307, USA*
[6]*National Center for Supercomputing Applications, University of Illinois at Urbana-Champaign, Urbana, Illinois 61801, USA*

(Received 2 May 2020; accepted 27 July 2020; published 18 August 2020)

Magnetocrystalline anisotropy is a fundamental property of magnetic materials that determines the dynamics of magnetic precession, the frequency of spin waves, the thermal stability of magnetic domains, and the efficiency of spintronic devices. We combine torque magnetometry and density functional theory calculations to determine the magnetocrystalline anisotropy of the metallic antiferromagnet Fe_2As. Fe_2As has a tetragonal crystal structure with the Néel vector lying in the (001) plane. We report that the fourfold magnetocrystalline anisotropy in the (001) plane of Fe_2As is extremely small, $K_{22} = -150\,\mathrm{J/m^3}$ at $T = 4\,\mathrm{K}$, much smaller than the perpendicular magnetic anisotropy of ferromagnetic structure widely used in spintronic devices. K_{22} is strongly temperature dependent and close to zero at $T > 150\,\mathrm{K}$. The anisotropy K_1 in the (010) plane is too large to be measured by torque magnetometry and we determine $K_1 = -830\,\mathrm{kJ/m^3}$ using first-principles density functional theory. Our simulations show that the contribution to the anisotropy from classical magnetic dipole-dipole interactions is comparable to the contribution from spin-orbit coupling. The calculated fourfold anisotropy in the (001) plane K_{22} ranges from -290 to $280\,\mathrm{J/m^3}$, the same order of magnitude as the measured value. We used K_1 from theory to predict the frequency and polarization of the lowest frequency antiferromagnetic resonance mode and find that the mode is linearly polarized in the (001) plane with $f = 670\,\mathrm{GHz}$.

DOI: 10.1103/PhysRevB.102.064415

I. INTRODUCTION

Antiferromagnets (AFs) have potential advantages over ferromagnets for spintronic devices. Collinear AFs are relatively insensitive to external fields because the net magnetization is zero. AFs typically have much higher antiferromagnetic resonance (AFMR) frequency than ferromagnets and therefore precessional switching can occur in AFs at a faster rate than in ferromagnets.

The recent discovery of *electrical* manipulation and detection of spin configurations in metallic AFs has led to a rapidly expanding scientific literature on this class of magnetic materials. Tetragonal crystals with easy-plane magnetic anisotropy are preferred because the two degenerate orientations of the Néel vector can store binary information. In crystals with globally centrosymmetric but locally noncentrosymmetric magnetic structures—e.g., CuMnAs and Mn_2Au—an electrical current exerts a torque on the Néel vector and the domain structure can potentially be switched electrically [1–4].

A small value of the in-plane magnetocrystalline anisotropy facilitates electrical switching of the domain orientation since a smaller torque is needed to overcome the energetic barrier that separates the two orientations. Thermal stability of the domain requires, however, a large value of the in-plane anisotropy. The Néel-Arrhenius law provides an estimate of the rate of thermal fluctuations of a single domain [5]:

$$\frac{1}{\tau} = f_0 \exp\left(-\frac{\Delta E}{k_B T}\right), \tag{1}$$

where τ is the average time between thermally activated changes in the direction of the magnetization, f_0 is the resonance frequency, ΔE is the energy barrier between two degenerate magnetic states, and $k_B T$ is the thermal energy. ΔE is given by the product of an anisotropy parameter K and the volume of the domain V; $\Delta E = KV$. Stable data storage typically requires $\Delta E/k_B T > 40$ to meet the criteria that data must be retained for 10 years [6].

For the media of conventional hard drives, the anisotropy parameter K is controlled by the perpendicular magnetocrystalline anisotropy of ordered intermetallic alloys. In the emerging technology of magnetic random access memory (MRAM), K is controlled by the interfacial magnetic anisotropy of a ferromagnetic layer adjacent to the oxide barrier in a magnetic tunnel junction. The perpendicular magnetic anisotropy K_1 of MRAM materials is typically $10^6 < K_1 < 10^7\,\mathrm{J\,m^{-3}}$ [7].

Magnetocrystalline anisotropy E_{ani} is described by a phenomenological expansion of the energy as a function of

*d-cahill@illinois.edu
†zhu.diao@famu.edu

direction cosines for the orientation of magnetization of a ferromagnet or the sublattice magnetization of an antiferromagnet (AF). For a tetragonal crystal, the expansion to fourth order gives three coefficients: K_1, K_2, and K_{22} [8]. K_1 is a second-order coefficient; K_2 and K_{22} are fourth-order coefficients,

$$E_{\text{ani}}/V = K_1 \sin^2\phi + K_2 \sin^4\phi + K_{22} \sin^4\phi \cos(4\theta), \quad (2)$$

where ϕ is the angle of the magnetization relative to the $\langle 001 \rangle$ direction and θ is the angle of the magnetization relative to the $\langle 100 \rangle$ direction (Fig. 2). The coefficient K_1 describes the twofold anisotropy in the (010) plane and K_2 represents the higher-order fourfold symmetry of the (010) plane. Because the effect of K_2 is usually much smaller than K_1, K_2 will be neglected in the following discussion. A crystal with an easy-plane anisotropy is described by $K_1 < 0$. The coefficient K_{22} describes the fourfold anisotropy of the (001) plane and determines the thermal stability of an easy-plane domain structure.

An external magnetic field applied to an antiferromagnet (AF) produces a small induced magnetic moment. The induced moment is small because tilting of the orientation of sublattice magnetization is constrained by strong exchange interaction between the magnetic sublattices that favors a parallel alignment of the sublattices. In general, however, the induced magnetic moment is not parallel to the applied field because magnetocrystalline anisotropy favors an orientation of the sublattice magnetization along an easy axis [9,10].

The lack of alignment between the induced moment $\boldsymbol{m}$ and the applied field $\boldsymbol{B}$ produces a macroscopic torque on the sample, $\boldsymbol{\tau} = \boldsymbol{m} \times \boldsymbol{B}$. A torque magnetometer measures this torque. Data for the torque as a function of applied field is sensitive to magnetocrystalline anisotropy as long as the anisotropy is neither too small nor too large. If the anisotropy is small, then the angle between $\boldsymbol{m}$ and $\boldsymbol{B}$ is small and the torque becomes difficult to detect. If the anisotropy is large, then the direction of $\boldsymbol{m}$ is fixed with respect to the crystallographic axis and the torque does not provide information about the magnitude of the anisotropy. We can measure the in-plane fourfold anisotropy of a mm-size bulk crystal of Fe_2As by torque magnetometry but the out-of-plane twofold anisotropy is not accessible to this technique because the external field is too small in comparsion to the anisotropy field to extract information about the anisotropy in the out-of-plane direction. We instead employ first-principles calculations based on density functional theory to determine K_1.

When magnetic energy is larger than the anisotropy energy, the amplitude of the torque in the (001) plane saturates and the fourfold magnetic anisotropy K_{22} can be directly determined from the amplitude of the torque. We measured three samples extracted from the same growth run, and the K_{22} value of all three samples is comparable to $-150\,\text{J/m}^3$ at 4 K. The magnitude of K_{22} drops quickly as temperature increases and reaches a small value above 150 K. The temperature dependence of magnetic anisotropy for antiferromagnets is similar to that of ferromagnets, following a power law of sublattice magnetization [11–13].

Strikingly, torque data for the applied field rotating in the (010) plane reveal the motion of domain walls. An applied field in the (010) plane of 1 T is sufficient to orient the Néel vector fully perpendicular to the applied field. Domain-wall motion occurs even at $T = 4$ K and, therefore, is not thermally activated.

In the final section, we derive the lowest, zone-center AFMR frequency for easy-plane AFs, $\omega = |\gamma|\sqrt{2H_E(H_{22} - H_1)} \approx |\gamma|\sqrt{-2H_E H_1}$, where γ is the gyromagnetic ratio, and H_E, H_1, H_{22} are the exchange field, out-of-plane anisotropy field, and in-plane anisotropy field, respectively. The anisotropy fields are calculated with anisotropy energy and sublattice magnetization: $H_1 = K_1/M$ and $H_{22} = K_{22}/M$. With K_1 calculated by DFT as $K_1 = -830\,\text{kJ/m}^3$, the AFMR frequency is $f = 670$ GHz at 4 K.

II. METHODS

Fe_2As crystallizes in the Cu_2Sb tetragonal crystal structure. Based on the corresponding magnetic symmetry (*mmm*1' magnetic point group), the Néel vector of Fe_2As has two degenerate orientations in the (001) plane [14–16].

The Fe_2As crystal was synthesized by mixing Fe and As powders in a 1.95:1 ratio and vacuum sealing inside a quartz tube. The vacuum tube was heated at 1 °C/min up to 600 °C and held for 6 h in a furnace. The temperature was then ramped to 975 °C at 1 °C/min and held for 1 h before cooling down slowly to 900 °C at 1 °C/min. Finally, the quartz tube was kept at 900 °C for 1 h and allowed to cool down to room temperature in the furnace at 10 °C/min. We obtained a large silver-hued crystal ingot of Fe_2As and it easily detached from the quartz tube. Part of the ingot was crushed into powder for powder XRD characterization and the data showed phase pure Fe_2As. But the sample is slightly off-stochiometry as described in Ref. [17]. The remaining portion of the ingot was then fractured and the fractured surface revealed a smooth facet. Laue diffraction was carried out after polishing this fractured surface. A fourfold symmetry pattern was observed indicating that the fractured surface is the (001) plane.

We used a wire saw to cut the sample into smaller pieces for magnetic property characterization and torque measurements. One of the pieces was measured on the superconducting quantum interference device vibrating sample magnetometer (SQUID VSM; see below), the other three pieces were used in torque magnetometry measurements. We name these three samples measured by torque magnetometry samples A–C, and the one for SQUID VSM is named sample D. We confirmed the Néel temperatures of samples A–C with differential scanning calorimetry (DSC) to be 352, 353, and 353 K, respectively. During the DSC measurement, each sample was heated from 393 to 493 K, then cooled from 493 to 393 K at a rate of $10\,\text{K min}^{-1}$. Each sample exhibited a 2–3 K hysteresis in critical temperature between warming and cooling cycles. We averaged the critical temperatures measured during heating and cooling to determine the Néel temperatures listed above.

The temperature-dependent magnetic susceptibility was measured with a SQUID VSM in a Quantum Design Magnetic Properties Measurement System (MPMS). The susceptibility of the sample was measured while cooling from 398 to 4 K in a 10-mT field.

Torque measurements were performed in a Quantum Design Physical Property Measurement System (PPMS). We mounted the sample on a standard torque sensor chip, P109A from Quantum Design with a sensitivity of 1×10^{-9} N m.

The PPMS horizontal sample rotator was used to control the angle between the crystal and the applied field. During the measurement, the external field rotated in either the (010) plane or the (001) plane, while the field-induced moment resided in the same plane as the rotating applied field. We detected the torque component, $\boldsymbol{m} \times \boldsymbol{B}$, that is perpendicular to this plane. Samples A–C were mounted on the cleaved (001) plane when the applied field was rotating in the (010) plane, and samples were mounted on the wire-cut (010) plane when the field was rotating in the (001) plane. The misorientation of samples mounted on the wire-cut (010) plane was judged to be less than 5°, based on the amplitude of twofold symmetry of torque data for the (001) plane. The amplitude of twofold symmetry component of the torque data for the (001) plane is shown in Fig. S2 and our calculation of the misorientation is also discussed in the Supplemental Material [18].

We performed first-principles DFT simulations using the Vienna *Ab Initio* Simulation Package (VASP) [19,20], to calculate the twofold anisotropy K_1 and obtain an estimate for the fourfold anisotropy K_{22}. The projector augmented wave (PAW) method [21] is used to describe the electron-ion interaction. Kohn-Sham states are expanded into plane waves up to a kinetic-energy cutoff of 600 eV. The Brillouin zone is sampled by a $21 \times 21 \times 7$ Monkhorst-Pack [22] (MP) **k**-point grid and the total energy is converged self-consistently to within 10^{-9} eV. The local density approximation (LDA) [23] and the generalized-gradient approximation developed by Perdew, Burke, and Ernzerhof (PBE) [24] are used to describe the exchange-correlation energy function, and results from the two different computational strategies are compared.

Achieving the extremely high accuracy for total energies that is required to compute the (001) plane magnetocrystalline anisotropy that is on the order of μeV per magnetic unit cell is numerically challenging; the required convergence parameters render it computationally too expensive to perform such calculations fully self-consistently. Instead, we use the convergence parameters quoted above to compute Kohn-Sham states, electron density, and relaxed atomic geometries for collinear magnetism and take noncollinear magnetism and spin-orbit coupling [25] into account without self-consistency of the Hamiltonian, as described in Ref. [26].

III. RESULTS AND DISCUSSION

A. Magnetic susceptibility and domain-wall motion

We use data for the magnetic susceptibility as input for modeling the torque magnetometry data and to provide insight into the reorientation of antiferromagnetic domains in an external magnetic field. Figure 1(a) summarizes the results for the magnetic susceptibility in the limit of small field. We fixed the applied field at 10 mT, along the ⟨100⟩ or ⟨001⟩ direction, measured the induced magnetic moment while cooling from $T = 398$ K, and calculated the susceptibility, $\chi = M/H$, where M is the magnetization. The measured susceptibility is similar to that in a prior report [14].

When the applied field is along an easy axis, we must take domain-wall motion into account. We assume that a 10-mT external field is too weak to significantly affect the domain structure. We further assume that the magnetic moment generated by an applied field along the ⟨100⟩ direction (the a axis of the crystal) has equal contributions from two types of domains that we label as D1 (Néel vector along ⟨100⟩) and D2 (Néel vector along ⟨010⟩) as illustrated in Fig. 2. For an applied field in the (001) plane, we define the susceptibility parallel to the Néel vector as $\chi_\parallel$ and that perpendicular to the Néel vector as $\chi'_\perp$. On the other hand, the susceptibility for an applied field in the ⟨001⟩ direction is defined as $\chi_\perp$. We expect $\chi'_\perp$ and $\chi_\perp$ to be similar but due to the tetragonal symmetry of the crystal structure, $\chi'_\perp$ and $\chi_\perp$ are not necessarily equal. We show below that the difference between $\chi_\perp$ and $\chi'_\perp$ is less than 5%.

Measurements of the magnetization as a function of field, see Fig. 1(b), show that χ_c is constant for H applied along the c axis. For H along the a axis, χ_a increases with field at low field, and is approximately constant for an applied field > 1 T. We attribute the field dependence of χ_a to domain-wall motion and the consequent evolution of the populations of domains

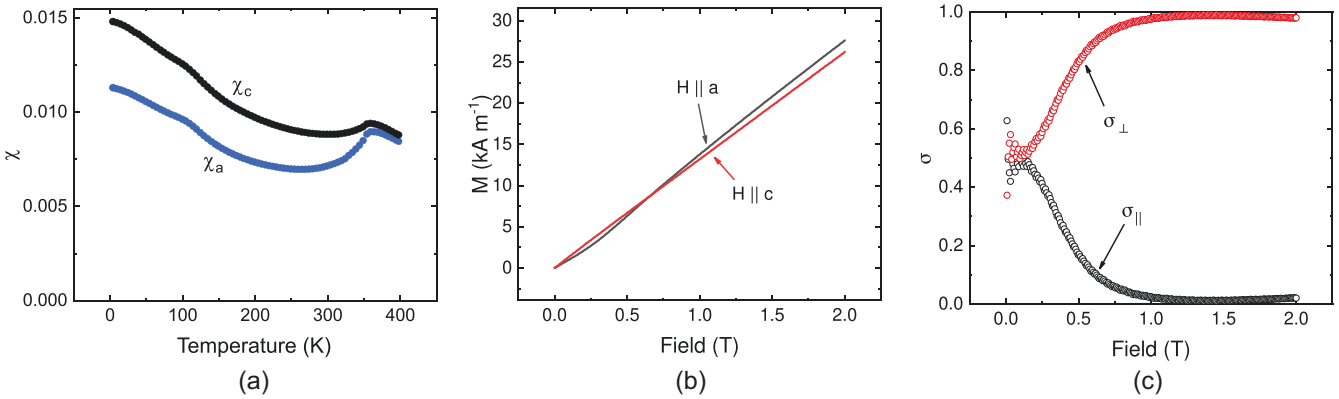

FIG. 1. (a) Temperature dependence of the magnetic susceptibility of Fe_2As in the low-field limit as measured using 10-mT field applied along the a axis (blue data points) and c axis (black data points) of the crystal. (b) Dependence of Fe_2As magnetization M on applied field H at $T = 4$ K. With H along the c axis (red line), M is a linear function of H. With H along the a axis (black curve), the nonlinear dependence of M on H is due to the rotation of antiferromagnetic domains. (c) The population of domains with Néel vectors parallel and perpendicular to the applied field estimated from the dependence of M on H. The assumptions are (1) in zero field, the population of domains with Néel vectors in the a and b directions are equal, and (2) in the high-field limit, the Néel vector is perpendicular to the applied field.

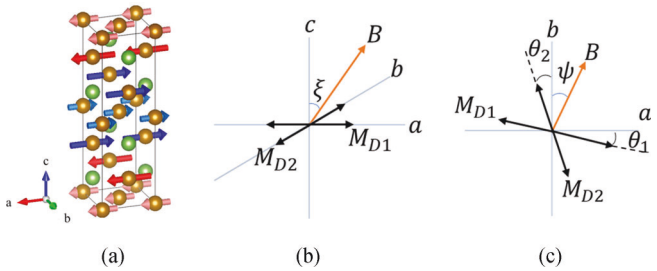

FIG. 2. Geometry of the torque magnetometry experiments. The *a*-*b*-*c* coordinates are the crystal axes. M_{D1} and M_{D2} are the sublattice magnetizations of the two types of domains labeled as D1 and D2. (a) The magnetic unit cell of Fe_2As. (b) Three-dimensional perspective of the measurement with the magnetic field rotating in the *ac* plane. The magnetic field makes an angle ξ with the *c* axis of the crystal. M_{D1} and M_{D2} are assumed to stay along the *a* and the *b* axis, respectively. The torque is along the *b* axis. (c) Plan view of the measurement with the magnetic field rotating in the *ab* plane. The magnetic field makes an angle ψ with the *b* axis of the crystal. M_{D1} and M_{D2} tilt away from *a* and *b* axis by θ_1 and θ_2, respectively (θ_1 and θ_2 are not necessarily the same). The torque is along the *c* axis (normal to the plane of the drawing).

with Néel vectors parallel and perpendicular to the applied field.

The populations of the two degenerate domains can be estimated from the M vs H curve in Fig. 1(a) by expressing the field-induced magnetization as $M_a = \sigma_\perp \chi'_\perp H + \sigma_{||}\chi_{||}H$ and $M_c = \chi_\perp H$, where $\sigma_\perp$ and $\sigma_{||}$ are the normalized domain fraction perpendicular and parallel to the *a* axis, respectively, and $\sigma_\perp + \sigma_{||} = 1$. We made three assumptions: (1) $\sigma_\perp = \sigma_{||} = 0.5$ at zero field; (2) $\sigma_\perp \approx 1$ at high field; and (3) domain-wall motion is reversible. The field-dependent distributions of domains parallel and perpendicular to the external field along the *a* axis at $T = 4$ K are shown in Fig. 1(c) and are treated as free parameters; we find $\chi_\parallel = 0.008$ and $\chi'_\perp = 0.018$. For an ideal collinear antiferromagnet, we expect $\chi_\parallel = 0$ at low temperatures [9]. This is not what we observed in our measurements. The reason is that there is a background contribution to the magnetic susceptibility that we do not yet understand. We assume that the background susceptibility is isotropic.

B. Torque magnetometry

The field-induced torque is the cross product of the field-induced magnetic moment and the applied field, $\boldsymbol{\tau} = \boldsymbol{m} \times \boldsymbol{B}$. The direction of the induced magnetic moment $\boldsymbol{m}$ is given by the minimum in the total energy: $E_{\rm tot} = E_m + E_{\rm ani} + E_{\rm ex}$, where E_m is the magnetic energy, $E_{\rm ani}$ is the magnetocrystalline anisotropy energy, and $E_{\rm ex}$ is the exchange energy that couples the two sublattices. We refer to the condition $E_m \ll E_{\rm ani}$ as the low-field limit and the condition $E_m \geqslant E_{\rm ani}$ as the intermediate-field regime [27]. We ignore a separate $E_{\rm ex}$ term when we analyze the torque data in the (001) plane because we assume that the exchange interaction stays the same and can be represented by susceptibility. For torque data in the (010) plane, our analysis is based on the anisotropy in the susceptibility, $\chi_\perp - \chi_{||}$, which is also related to the strength of the exchange interaction.

Figure 2(a) shows the experimental geometry when the applied field is rotating in the (010) plane. ξ is the angle between the *c* axis and the applied field. The induced moments are also in the (010) plane. Thus, the torque is along the ⟨010⟩ direction. In the low-temperature limit, $\chi_{||} = 0$ if the isotropic background is ignored; the induced moment of domain D1 is therefore along ⟨001⟩ and the induced moment of D2 lies in the (010) plane between ⟨001⟩ and ⟨100⟩. The direction of the induced moment of D2 is determined by $\chi_\perp$ and $\chi'_\perp$.

Figure 2(b) shows the experimental geometry when the applied field is rotating in the (001) plane. In this case, because of the relatively small magnetocrystalline anisotropy, the tilt of the sublattice magnetization away from the crystal axes is significant. ψ is the angle between the external field and the crystal axes; θ_1, θ_2 are the angles between the directions of the sublattice magnetization of domains D1, D2 and the crystal axes, respectively (θ_1 and θ_2 are not necessarily equal).

1. Torque magnetometry in the (010) plane in the low-field limit

The torque is zero when the applied field is along the easy or hard axis of a sample, because the induced magnetization is in the same direction as the field. Here, we refer to the easy axis as the lowest energy orientation of the Néel vector, and define orientations of the hard axis as perpendicular to the easy axis. When the applied field is oriented away from an easy or hard axis, the direction of the induced magnetization shifts toward a hard axis because $\chi_\perp > \chi_{||}$. In an AF, the slope of the torque as a function of field orientation has opposite signs when the field passes through the orientation of an easy axis and when it passes through the orientation of a hard axis. In our sign convention, torque with a negative slope as a function of angle indicates a hard axis; torque with a positive slope as a function of angle indicates an easy axis. In a single magnetic domain of Fe_2As, there are two hard axes: the *c* axis perpendicular to the (001) plane and the axis perpendicular to the Néel vector in the (001) plane.

Torque data at 4 K with the field rotating in the (010) plane are shown in Fig. 3(a). The slope when the field is along the *a* axis ($\xi = 90°$) is positive at $B = 0.5$ T and changes to negative at $B > 0.5$ T. Therefore, when the 0.5-T field is oriented along the *a* axis, the *a* axis is an easy axis but when B is greater than 0.5 T, the *a* axis becomes a hard axis. This interpretation is consistent with the analysis of the domain distribution discussed above and displayed in Fig. 1(c). When the applied field along the *a* axis is larger than 1 T, the majority of domains are in the D2 configuration and the *a* axis becomes a hard axis.

The slope of torque data when the applied field is along the *c* axis ($\xi = 0°$) is negative because the *c* axis is a hard axis. However, when $\xi = 10°$ and $B > 0.5$ T, the sign of the torque changes abruptly. This dramatic change in the sign of the torque is periodic; the periodicity indicates that domain-wall motion is reversible. When the applied field is aligned along the *c* axis, the populations of domain D1 and D2 are equal. As the field rotates away from the *c* axis, the projection of the applied field in the (001) plane changes the domain distribution as described by Fig. 1(c). When the field returns to the *c* axis, the populations of domain D1 and domain D2 become equal again.

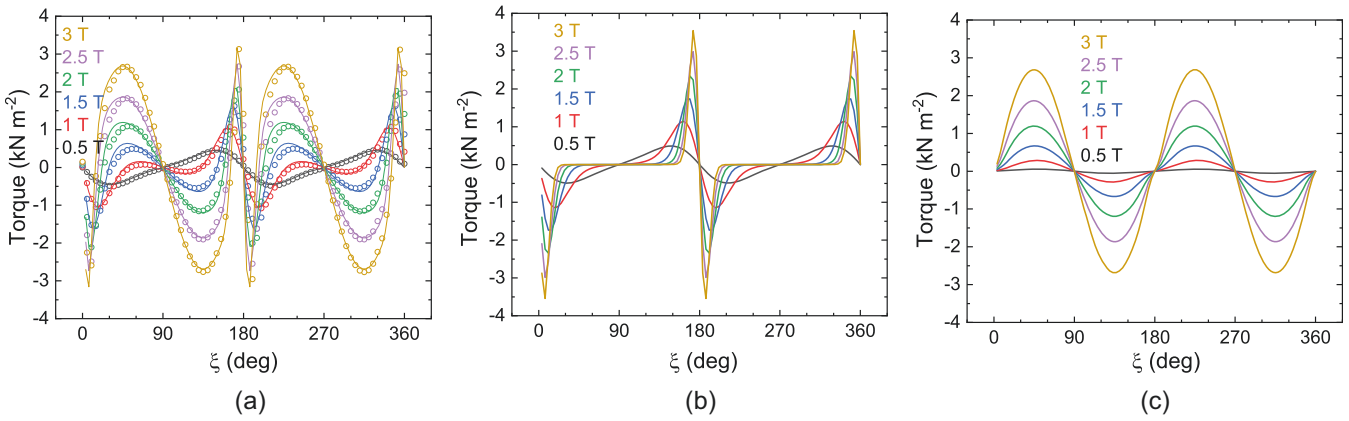

FIG. 3. (a) Torque magnetometry measurements in the *ac* plane of Fe_2As at $T = 4$ K. Open symbols are measured data; solid lines are fits to the data. The legend gives the magnitude of the applied field labeled by color. (b) Calculated torque generated by domains of type D1 as a function of applied field. (c) Calculated torque generated by domains of type D2 as a function of applied field.

To model the torque data, we first calculate the direction and magnitude of the induced magnetization $\boldsymbol{M}$ by describing the susceptibility as a tensor $M_i = \sum_j \chi_{ij} H_j$ [8]. As shown in Fig. 2(a), there are two degenerate domains with their Néel vectors perpendicular to each other. For domains of type D1, the Néel vector is along the a axis and the susceptibility tensor is

$$\chi_{\mathrm{D1}} = \begin{pmatrix} \chi_{||} & 0 & 0 \\ 0 & \chi'_{\perp} & 0 \\ 0 & 0 & \chi_{\perp} \end{pmatrix}. \tag{3}$$

For domains of type D2, the Néel vector is along the b axis and the susceptibility tensor is

$$\chi_{\mathrm{D2}} = \begin{pmatrix} \chi'_{\perp} & 0 & 0 \\ 0 & \chi_{||} & 0 \\ 0 & 0 & \chi_{\perp} \end{pmatrix}. \tag{4}$$

The external field in the (010) plane is $H = H_0[\ \sin(\xi)\quad 0\quad \cos(\xi)\ ]^T$, where ξ is the angle between the c axis and the external field as depicted in Fig. 2(a). We consider the effect of the projection of the applied field along the a axis $H_0\sin(\xi)$ on the domain distribution as described by the data of Fig. 1(c). The torque signals of two types of domains are $\boldsymbol{\tau}_{\mathrm{D1}}/V = \sigma_{\mathrm{D1}}\chi_{\mathrm{D1}}\boldsymbol{H}\times\boldsymbol{B}$ and $\boldsymbol{\tau}_{\mathrm{D2}}/V = \sigma_{\mathrm{D2}}\chi_{\mathrm{D2}}\boldsymbol{H}\times\boldsymbol{B}$, while the total torque is the sum $\boldsymbol{\tau}_{\mathrm{D1}} + \boldsymbol{\tau}_{\mathrm{D2}}$. To evaluate this model, we use the measured magnetic susceptibility as shown in Fig. 1. The free parameters are $\chi'_{\perp}/\chi_{\perp}$ and $\chi_{||}$.

Figures 3(b) and 3(c) show the calculated values of τ_{D1} and τ_{D2}; the solid lines in Fig. 3(a) are the summation of the two. The good correspondence between the model and the data supports our assertion that domain-wall motion is reversible.

The difference in the sign of τ_{D1} and τ_{D2} contributes to the abrupt change in the torque signal near an angle of 10°. For D1 domains, when the applied field is rotating in the (010) plane, the induced moment is always close to the c axis because $\chi_{||}$ is small. For D2 domains, the field-induced magnetization is $M = H_0[\ \chi'_{\perp}\sin(\xi)\quad 0\quad \chi_{\perp}\cos(\xi)\ ]^T$. If $\chi'_{\perp} = \chi_{\perp}$, the induced magnetization $M = \chi_{\perp}H_0[\ \sin(\xi)\quad 0\quad \cos(\xi)\ ]^T$ would be parallel to the applied field H. This would infer that there is no torque signal from D2 domains and the total torque signal would be generated only by D1 domains [Fig. 3(b)].

However, the total torque signal we observe is obviously different from what is depicted in Fig. 3(b) (D1 domains only). The torque signal resembles a combination of two domains, hence, we can conclude $\chi'_{\perp} \neq \chi_{\perp}$. On the other hand, the dramatic change in the sign of the total torque signal at $\xi = 10^{\circ}$ and $T = 4$ K indicates that $\boldsymbol{\tau}_{\mathrm{D1}}$ and $\boldsymbol{\tau}_{\mathrm{D2}}$ have opposite signs. Since the induced moment of D1 domains is along the c axis, the induced moment of D2 domains must be between the applied field and the a axis.

The difference between $\chi_{\perp}$ and $\chi'_{\perp}$ is also observed in the dependence of M on H [Fig. 1(b)]. Figure 4(a) shows the difference between M_c and M_a as a function of applied field and temperature. The bump of $M_c - M_a$ at room temperature and below is due to domain-wall motion; the difference at high fields is a result of $\chi_{\perp} - \chi'_{\perp}$.

The magnetization of D2 domains in the (010) plane experiences an anisotropic environment that originates from the difference of the a and c axes of the crystal. By fitting the model to the torque data, we determine $\chi'_{\perp} - \chi_{\perp}$ as a function of temperature [Fig. 4(b)]. We observe a change in the sign of $\chi_{\perp} - \chi'_{\perp}$ near 200 K that is consistent with the anisotropy in the dependence of M on H [Fig. 4(a)]. This change in sign indicates that the field-induced magnetization of D2 domains is between the applied magnetic field and the a axis below 200 K, and between the applied magnetic field and the c axis above 200 K. The anisotropy in the perpendicular susceptibility, $\chi_{\perp} - \chi'_{\perp}$, is always small compared to its absolute value, $|\chi_{\perp} - \chi'_{\perp}|/\chi_{\perp} \leqslant 0.05$.

2. Torque magnetometry in the (001) plane under intermediate field

Figure 5(a) shows torque data acquired with the applied field rotating in the (001) plane. As expected, the data show fourfold symmetry. We attribute the small twofold symmetry to a background that comes from misalignment of the sample. (The c axis is not precisely perpendicular to the field direction.) The amplitude of the fourfold contribution to the torque as a function of applied field of three samples from the same growth run at 4 K is plotted in Fig. 5(b). The fourfold

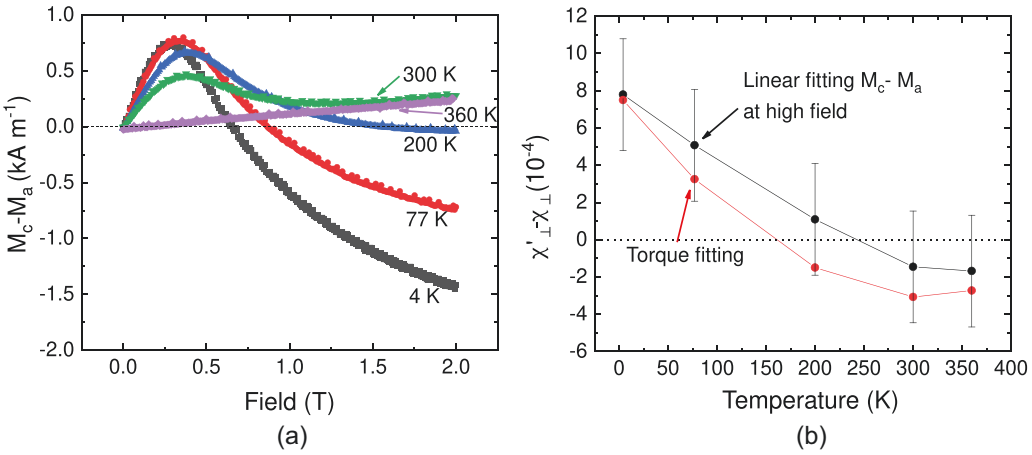

FIG. 4. (a) The field dependence of the difference $M_c - M_a$ between the magnetization with an applied field along the c direction M_c and the field applied along the a direction M_a. Each curve is labeled by the measurement temperature. When the applied field along the a axis is larger than 1.5 T, all domains can be treated as equivalent to M_{D2}. Therefore, the slope of the data for magnetic fields larger than 1.5 T is the difference in the susceptibility $\chi_\perp - \chi'_\perp$, where $\chi'_\perp$ is the susceptibility in the ab plane perpendicular to M_{D2} and $\chi_\perp$ is the susceptibility along the c axis perpendicular to M_{D2}. (b) Comparison of the temperature dependence of $\chi'_\perp - \chi_\perp$ value from direct measurements of the type shown in (a) and from fitting the torque data.

amplitude at higher temperature of three samples can be found in Fig. S1 of the Supplemental Material [18].

To quantify the magnetic anisotropy in the (001) plane of Fe_2As, we analyze the torque data by minimizing the total energy for D1 and D2 domains, respectively, then add τ_{D1} and τ_{D2} together to compare it to the data. When E_m is comparable to or larger than E_{ani} ($E_m \geqslant E_{ani}^{(001)}$), Néel vectors start tilting away from crystal axes as shown in Fig. 2(b). We assume that the two sublattice magnetizations are approximately parallel to each other, so the exchange interaction is considered in magnetic energy. With the applied field rotating in the (001) plane of Fe_2As, the total energy is

$$E_{tot}/V = -\tfrac{1}{2}H(\psi)\chi_{tot}(\psi,\theta)H^T(\psi) + K_{22}\cos(4\theta) + K_1 + K_2, \quad (5)$$

where $\chi_{tot} = \sigma_{D1}\chi_{D1}$, $\theta = \theta_1$ for D1 domains and $\chi_{tot} = \sigma_{D2}\chi_{D2}$, $\theta = \theta_2$ for D2 domains.

To obtain an accurate value of E_m, we rotate the susceptibility tensor together with the Néel vector, $\chi^R(\theta) = R(\theta)\chi R^T(\theta)$ [8], where θ is the angle between the Néel vector and the crystal axis, and $R(\theta)$ is the rotation matrix:

$$R(\theta) = \begin{pmatrix} \cos(\theta) & -\sin(\theta) & 0 \\ \sin(\theta) & \cos(\theta) & 0 \\ 0 & 0 & 1 \end{pmatrix}. \quad (6)$$

During the rotation, the field component along M_{D1} and M_{D2} result in a change in the populations of D1 and D2 domains. Thus, σ_{D1} and σ_{D2} are determined by the angle between the applied field and the spin axis.

The analogous behavior of a uniaxial antiferromagnet (AF) [10] provides a point of comparison. In a uniaxial AF, the critical field for the spin-flop transition is $H_c = \sqrt{2(K_1 + K_2)/(\chi_\perp - \chi_\parallel)}$. For Fe_2As, as shown in Figs. 1(c) and 5(b), we do not observe a sudden change in the

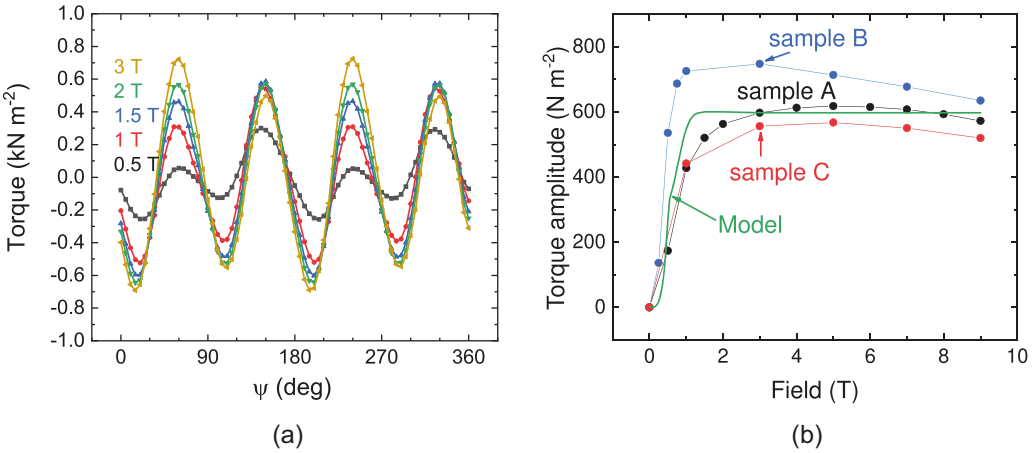

FIG. 5. (a) Torque magnetometry measurements of Fe_2As (sample A) in the ab plane at $T = 4$ K. (b) The amplitude of the fourfold component of the torque extracted from measurements of the type shown in panel (a) at $T = 4$ K and compared to an analytical model (see text). When amplitude of the fourfold component of the torque saturates at the value τ_0, the in-plane anisotropy is $\tau_0 \approx 4K_{22}$.

domain populations that would be characteristic of a spin-flop transition. Furthermore, in a perfect crystal that is free from disorder, the single domain structure created by an applied field would persist after the field is removed. (In ferromagnets, domains form to reduce the contribution of the magnetic energy of stray fields to the total energy. In AFs, this driving force for domain formation is absent.) We attribute gradual and reversible domain movement in Fe_2As to random strain fields created by static disorder in the crystal that lead to local variations in the anisotropy energy.

The midpoint of the change in the populations of the D1 and D2 domains as a function of field is, however, close to what is expected for the characteristic field of a spin-flop transition of an ideal single domain easy-plane antiferromagnetic crystal. The total energy of D2 when $\xi = 90^\circ$ is [8]

$$\frac{E_{\text{tot}}}{V} = K_1 + K_2 + K_{22}\cos(4\theta_2) + \frac{1}{2}(\chi_\perp - \chi_{||})H^2\cos^2(\psi + \theta_2) - \frac{1}{2}\chi_\perp H^2. \quad (7)$$

Both anisotropy and magnetic energy are functions of θ_2 but with different periodicity. For an applied field along the $\langle 010\rangle$ direction ($\psi = 0^\circ$), $E_{\text{tot}}(\theta_2 = 90^\circ)$ is always a global minimum while $E_{\text{tot}}(\theta_2 = 0^\circ)$ is at a local minimum under low fields and it becomes the global maximum when the applied field is larger than a characteristic field H_c. We can derive this critical field from $\theta_{\max} = \frac{1}{2}\arccos\frac{(\chi_\perp - \chi_{||})H^2}{16|K_{22}|}$ in which $\theta_{\max}$ represents the spin orientation when total energy is at the global maximum under a known applied field. When $H \geqslant H_c$, $\theta_{\max}(H \geqslant H_c) = 0^\circ$. Therefore, $\mu_0 H_c = \sqrt{16|K_{22}|/(\chi_\perp - \chi_{||})} = 560$ mT using the value of $K_{22} = -150\,\text{J/m}^3$ from our torque magnetometry measurement as described below.

We attribute our observations that domains begin to move in an applied field smaller than H_c and domain-wall motion is not complete until the applied field is larger than H_c to an inhomogeneous distribution of local values of the magnetocrystalline anisotropy. We speculate that random strains in the crystal caused by point and extended defects create a relatively broad distribution of anisotropy at different locations in the sample. When the external field is removed, the random strain field controls the energy of the domain orientation and the volume fraction of domains recovers its initial states.

The torque induced by the applied field is the derivative of the total energy $\tau = dE_{\text{tot}}/d\psi$. In the intermediate-field regime, i.e., $E_m \geqslant E_{\text{ani}}$ or $H \geqslant H_c$, we assume that the sample is a single domain and the sublattice magnetization is always nearly perpendicular to the applied field, i.e., $\theta + \psi \approx \pi/2$. The "intermediate-field" regime refers to an applied field larger than the characteristic field, but not large enough to significantly change the exchange interaction. An important assumption here is that the tilt of the two sublattice magnetizations in the external field is small enough to be neglected. With this approximation, the magnetic energy is nearly independent of θ and ψ, $E_m \approx -\frac{1}{2}\chi_\perp H_0^2$. Then, the torque can be easily related to the anisotropy: $\tau = \frac{dE_{\text{tot}}}{d\psi} \approx \frac{dE_{\text{ani}}}{d\psi} = -4K_{22}\sin(4\psi)$, where τ no longer depends on the magnitude of the applied field.

A gradual reorientation of domains of an easy-plane antiferromagnet as a function of applied field was also recently observed in 50-nm-thick CuMnAs epitaxial layers grown on GaP [28]. (CuMnAs and Fe_2As have essentially the same crystal structure with Cu and Mn atoms in CuMnAs occupying the same lattice sites as the two crystallographically distinct Fe atoms in Fe_2As.) The strength of the field needed to reorient antiferromagnetic domains in CuMnAs epitaxial layers is similar to what we observe in Fe_2As bulk crystals. Thinner, 10-nm-thick CuMnAs layers show a pronounced in-plane uniaxial anisotropy and a more abrupt transition in domain structure as a function of field than 50-nm-thick layers. X-ray magnetic linear dichroism (XMLD) measurements of CuMnAs epitaxial layers reveal that the domain reorientation is not fully reversible and hysteretic for fields less than 2 T. X-ray photoelectron microscopy (XPEEM) images acquired after applying 7-T fields in orthogonal directions also show that the domain structure does not revert to a fixed configuration in zero field.

Based on our observation in Fig 5(b), as field increases, τ increases quickly then saturates. At higher fields, τ is slightly smaller than the saturation value, rather than staying the same until 9 T. At higher fields, the tilting of spins caused by the external field cannot be neglected, so exchange interaction is no longer a constant. In our model, however, the torque stays the same after saturation based on our assumption of constant susceptibility and exchange interaction. This assumption is no longer valid in higher field. While induced magnetization is smaller than χH, the torque is also smaller than the saturation value.

As our model predicts, the experimentally measured torque amplitude saturates as the applied field approaches 1 T for sample B, and 3 T for samples A and C. Hence, it is safe to select 1 and 3 T as the "intermediate-field" regime for sample B and for samples A and C, respectively. The measured K_{22} value of sample A is $-150\,\text{J/m}^3$. The field dependence of K_{22} in all three samples follows the same trend, however, individual data points do not overlap perfectly. To determine the error in the measurement of K_{22} when there is misalignment of the crystal, we introduced a 10° tilting of the susceptibility tensor in the model and calculated the error propagation. This 10° misorientation of susceptibility resulted in a 0.3% error in the simulated fourfold torque amplitude. Since the fourfold amplitude is linearly related to K_{22}, the error of K_{22} caused by a 10° misalignment is also 0.3%. We attribute the differences in K_{22} between the three samples to minor variations in the defect microstructures and stoichiometries of the three samples.

With a temperature-dependent measurement of torque in the *ab* plane at an intermediate field, we obtain the temperature dependence of K_{22} as shown in Fig. 6. The overall temperature dependence is similar for all three samples with relatively minor differences. As temperature increases, the magnitude of K_{22} decreases and becomes close to zero at $T > 150$ K. K_{22} of sample A becomes slightly positive for $T > 150$ K. From Eq. (2), the total energy reaches a minimum when the Néel vector is along the crystal *a* and *b* axes ($\theta = 0^\circ$ or $\pm 90^\circ$) for $K_{22} < 0$ at zero field. When $K_{22} > 0$, the Néel vector lies in directions with $\theta = \pm 45^\circ$ [8].

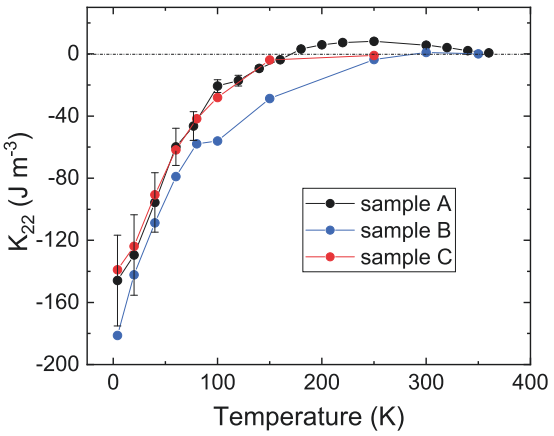

FIG. 6. Temperature dependence of in-plane magnetocrystalline anisotropy K_{22} of Fe_2As. The torque data with the external field rotating in the (001) plane were measured with an intermediate-field strength (3 T for sample A and sample C, and 1 T for sample B) and the amplitude of the fourfold symmetry was extracted to obtain the in-plane anisotropy with $\tau_0 \approx 4K_{22}$. Intermediate field is defined as a field strength under which the torque amplitude of fourfold symmetry saturates at 4 K. The error bars represent 20% uncertainty in determining the saturation value of the torque amplitude. All three samples have the same uncertainty, and we only plot error bars for sample A to make the plot more readable.

C. First-principles calculations of magnetocrystalline anisotropy

Magnetocrystalline anisotropy of Fe_2As has two contributions, one from spin-orbit interaction (SOI) and one from classical magnetic dipole-dipole interaction (MDD): anisotropy from SOI is calculated using DFT for noncollinear magnetism with spin-orbit coupling, by rotating the Néel vector both within the easy plane (001) and out of the plane towards the hard axis (in the (010) plane). The corresponding total-energy changes are visualized in Fig. S3 of the Supplemental Material [18] and the anisotropy energies are then obtained by fitting the energy change vs Néel vector orientation to Eq. (2). This leads to a twofold symmetric SOI anisotropy energy for the Néel vector in the (010) plane and a fourfold symmetric one for the (001) plane. In DFT-LDA, the (010) plane anisotropy energy is $K_1 = -320\,\mathrm{kJ/m^3}$ and $K_{22} = -290\,\mathrm{J/m^3}$ for the (001) plane. A nonzero K_{22} indicates the existence of two local energy minima. In DFT-PBE, the corresponding values are $K_1 = -530\,\mathrm{kJ/m^3}$ for the (010) plane and $K_{22} = 280\,\mathrm{J/m^3}$ for the (001) plane. The sign of K_{22} differing between DFT-LDA and DFT-PBE implies that the energetic ordering of these two minima is inverted. Negative K_{22} means that the energy minimum occurs for a Néel vector along a ⟨100⟩ equivalent direction and positive K_{22} for a Néel vector along a ⟨110⟩ equivalent direction.

The MDD contribution is computed using a classical model that is parametrized using the chemical and magnetic ground-state structure from DFT. We use the ground-state chemical and magnetic structure from DFT-LDA as well as DFT-PBE, to evaluate the following expression for the classical magnetic dipole-dipole interaction and to compare the influence of exchange and correlation:

$$E_d = -\frac{1}{2}\frac{\mu_0}{4\pi}\sum_{i\neq j}\frac{3[\boldsymbol{m}(\boldsymbol{r}_i)\cdot\boldsymbol{r}_{ij}][\boldsymbol{m}(\boldsymbol{r}_j)\cdot\boldsymbol{r}_{ij}]-[\boldsymbol{m}(\boldsymbol{r}_i)\cdot\boldsymbol{m}(\boldsymbol{r}_j)]r_{ij}^2}{r_{ij}^5} \tag{8}$$

To obtain the anisotropy energy for bulk Fe_2As from this expression, we use an interaction shell boundary r_{ij} of 180 Å, which converges the result to within 10^{-7} eV. This leads to a twofold symmetric MDD contribution to the anisotropy energy in the (010) plane of $K_1 = -220\,\mathrm{kJ/m^3}$ for LDA. For PBE, the corresponding value is $K_1 = -300\,\mathrm{kJ/m^3}$. The MDD contribution in the (001) plane is less than 1 neV and, thus, negligible.

Therefore, we find a total out-of-plane anisotropy energy of $-540\,\mathrm{kJ/m^3}$ and $-830\,\mathrm{kJ/m^3}$ from LDA and PBE, respectively. We attribute ∼2/3 of the total out-of-plane anisotropy energy to the SOI contribution and ∼1/3 to the MDD contribution. Both terms show twofold symmetry with the hard axis along the ⟨001⟩ direction. Torque magnetometry can only measure a lower bound of $|K_1| > 36\,\mathrm{kJ/m^3}$ for the out-of-plane anisotropy energy and does not contradict our DFT results.

The in-plane anisotropy energy is computed as $K_{22} = -290\,\mathrm{J/m^3}$ (DFT-LDA) and $K_{22} = 280\,\mathrm{J/m^3}$ (DFT-PBE), while the measured result is $K_{22} = -150\,\mathrm{J/m^3}$.

D. Antiferromagnetic resonance of easy-plane antiferromagnets

Without anisotropy, the magnon dispersion of energy in antiferromagnet is zero at the center of the Brillouin zone. Anisotropy introduces a band gap at the zone center. The antiferromagnetic resonance (AFMR) mode we refer to in this work describes this precessional magnetization motion at the zone center. With the anisotropy values we determined by theory and experiment, we can make an estimation of the AFMR frequency.

We start from equations of motion under the "macrospin" approximation of the two magnetic sublattices in domain D1 [29,30]:

$$\frac{dM_1}{dt} = |\gamma|M_1 \times \left[(H_{22}+H_{\mathrm{ex}})\hat{i} + \left(-\lambda M_2^b + \frac{M_1^b}{M}H_{22}\right)\hat{j} + \left(-\lambda M_2^c + \frac{M_1^c}{M}H_1\right)\hat{k}\right], \tag{9}$$

$$\frac{dM_2}{dt} = |\gamma|M_2 \times \left[(-H_{22}-H_{\mathrm{ex}})\hat{i} + \left(-\lambda M_1^b + \frac{M_2^b}{M}H_{22}\right)\hat{j} + \left(-\lambda M_1^c + \frac{M_2^c}{M}H_1\right)\hat{k}\right], \tag{10}$$

where γ is the gyromagnetic ratio, M_1 and M_2 are sublattice magnetizations of domain D1, H_1 and H_{22} are out-of-plane and in-plane anisotropy fields, respectively, which can be written as $H_1 = K_1/M$ and $H_{22} = K_{22}/M$. $H_{\mathrm{ex}} = \lambda M$ and λ

is the intersublattice exchange interaction. $M_1^a = -M_2^a \approx M$, M^b, and M^c are magnetization components along the b and the c axis, respectively, during spin procession.

Because the two sublattices along the a axis are aligned antiparallel to each other, the anisotropy fields along the a axis are of opposite signs. Along the b and c axes, the sign of the effective anisotropy field is determined by the signs of $M_{1,2}^b$ and $M_{1,2}^c$. In domain D1, although the sublattice magnetizations stay along the a axis, the in-plane anisotropy is of fourfold symmetry, so there is equivalent anisotropy energy contribution along the a and b axes. The effective anisotropy fields along the a and b axes are determined by the projection of magnetization on these axes.

The only nonzero solution of the equation of motion requires $M_1^b = M_2^b$ and $M_1^c = -M_2^c$, as shown in Fig. S4 of the Supplemental Material [18]. The corresponding angular frequency can be expressed as $\omega = |\gamma|\sqrt{2H_{\rm ex}(H_{22} - H_1)}$.

In easy-plane AFs, $K_1 < 0$ and its absolute value is usually much larger than K_{22}, thus the frequency is always real. Besides, the AFMR frequency is smaller with smaller $H_{22} - H_1$ value, because the system is more isotropic. For easy-plane materials with $|K_{22}| - |K_1| \ll 0$, the AFMR frequency is dominated by the anisotropy in the direction perpendicular to the easy plane.

For the exchange field, we use sublattice magnetization $M_{\rm D1} = 4 \times 10^5 {\rm A/m}$ and an exchange integral $\lambda \approx 1/\chi_\perp$ with calculated $\chi_\perp = 0.0036$. We obtain an exchange field $H_{\rm ex} \approx 140$ T. With calculated K_1 value from DFT-PBE, $K_1 = -830\,{\rm kJ/m^3}$, the AFMR frequency is $f = 670\,{\rm GHz}$.

For tetragonal antiferromagnets like Fe_2As, the AFMR is dominated by K_1 because $|K_1| \gg |K_{22}|$. The same relation is also valid for Mn_2Au where a previous calculation [31] shows that the magnitude of the out-of-plane anisotropy is also much larger than the in-plane anisotropy. It is important to determine K_1 to estimate AFMR frequency, and both K_1 and K_{22} values are needed for thermal stability of spintronic materials.

As discussed in Refs. [2] and [32], the electrical current typically switches only a small number of antiferromagnetic domains. As the anisotropy energy scales with sample volume, the total in-plane anisotropy energy is determined by the volumetric difference of the two kinds of domains, $\Delta E = (V_{\rm D1} - V_{\rm D2})K_{22}$. $V_{\rm D1} - V_{\rm D2}$ depends on temperature, current density, and the pulse width [33]. If the attempt frequency is high and $V_{\rm D1} - V_{\rm D2}$ is small, the magnetic state is more susceptible to thermal fluctuations.

IV. CONCLUSION

We performed torque magnetometry measurements on an easy-plane antiferromagnet Fe_2As. The measurement results prove that the domain-wall motion in the single-crystalline sample is reversible, and allow us to extract the in-plane anisotropy when the magnetic energy E_m is comparable to magnetocrystalline anisotropy energy $E_{\rm ani}$. The in-plane anisotropy of Fe_2As is $K_{22} = -150\,{\rm J/m^3}$ at 4 K. K_{22} is strongly temperature dependent and its magnitude decreases as a function of temperature. This means that the domain structure in Fe_2As may easily be perturbed by a small applied field at room temperature. With $K_1 = -830\,{\rm kJ/m^3}$ calculated from DFT, we derived the AFMR frequency $f = \frac{|\gamma|}{2\pi}\sqrt{2H_{\rm ex}(H_{22} - H_1)} = 670\,{\rm GHz}$. Our analysis of torque magnetometry data suggests that the in-plane magnetic anisotropy of some candidate materials for antiferromagnetic spintronic applications, such as Fe_2As, can be very small at room temperature. A field smaller than 1 T is sufficient to significantly alter its domain structure. The measurement of K_{22} in Fe_2As provides a baseline value for further studies of magnetic anisotropy of easy-plane antiferromagnets and the motion of antiferromagnetic domain walls.

ACKNOWLEDGMENTS

This work was undertaken as part of the Illinois Materials Research Science and Engineering Center, supported by the National Science Foundation MRSEC program under NSF Award No. DMR-1720633. This work made use of the Illinois Campus Cluster, a computing resource that is operated by the Illinois Campus Cluster Program (ICCP) in conjunction with the National Center for Supercomputing Applications (NCSA) and which is supported by funds from the University of Illinois at Urbana-Champaign. This research is part of the Blue Waters sustained-petascale computing project, which is supported by the National Science Foundation (Awards No. OCI-0725070 and No. ACI-1238993) and the state of Illinois. Blue Waters is a joint effort of the University of Illinois at Urbana-Champaign and its National Center for Supercomputing Applications. Z.D. acknowledges support from the Swedish Research Council (VR) under Grant No. 2015-00585, cofunded by Marie Skłodowska-Curie Actions (Project No. INCA 600398).

[1] P. Wadley, B. Howells, J. Železný, C. Andrews, V. Hills, R. P. Campion, V. Novák, K. Olejník, F. Maccherozzi, S. S. Dhesi, S. Y. Martin, T. Wagner, J. Wunderlich, F. Freimuth, Y. Mokrousov, J. Kuneš, J. S. Chauhan, M. J. Grzybowski, A. W. Rushforth, K. W. Edmonds *et al.*, Science **351**, 587 (2016).

[2] M. J. Grzybowski, P. Wadley, K. W. Edmonds, R. Beardsley, V. Hills, R. P. Campion, B. L. Gallagher, J. S. Chauhan, V. Novak, T. Jungwirth, F. Maccherozzi, and S. S. Dhesi, Phys. Rev. Lett. **118**, 057701 (2017).

[3] K. Olejník, T. Seifert, Z. Kašpar, V. Novák, P. Wadley, R. P. Campion, M. Baumgartner, P. Gambardella, P. Nemec, J. Wunderlich, J. Sinova, P. Kužel, M. Müller, T. Kampfrath, and T. Jungwirth, Sci. Adv. **4**, eaar3566 (2018).

[4] M. Meinert, D. Graulich, and T. Matalla-Wagner, Phys. Rev. Appl. **9**, 064040 (2018).

[5] H. J. Richter, J. Phys. D: Appl. Phys. **32**, R147(R) (1999).

[6] J. J. Nowak, R. P. Robertazzi, J. Z. Sun, G. Hu, J. H. Park, J. Lee, A. J. Annunziata, G. P. Lauer, R. Kothandaraman, E. J. O'Sullivan, P. L. Trouilloud, Y. Kim, and D. C. Worledge, IEEE Magn. Lett. **7**, 1 (2016).

[7] A. V. Khvalkovskiy, D. Apalkov, S. Watts, R. Chepulskii, R. S. Beach, A. Ong, X. Tang, A. Driskill-Smith, W. H. Butler,

P. B. Visscher, D. Lottis, E. Chen, V. Nikitin, and M. Krounbi, J. Phys. D: Appl. Phys. **46**, 074001 (2013).
[8] M. Herak, M. Miljak, G. Dhalenne, and A. Revcolevschi, J. Phys.: Condens. Matter **22**, 026006 (2010).
[9] J. M. D. Coey, *Magnetism and Magnetic Materials* (Cambridge University Press, Cambridge, UK, 2009) .
[10] U. Gäfvert, L. Lundgren, B. Westerstrandh, and O. Beckman, J. Phys. Chem. Solids **38**, 1333 (1977).
[11] C. Zener, Phys. Rev. **96**, 1335 (1954).
[12] J. C. Burgiel and M. W. P. Strandberg, J. Phys. Chem. Solids **26**, 877 (1965).
[13] P. Pincus, Phys. Rev. **113**, 769 (1959).
[14] H. Katsuraki and N. Achiwa, J. Phys. Soc. Jpn. **21**, 2238 (1966).
[15] H. Katsuraki and K. Suzuki, J. Appl. Phys. **36**, 1094 (1965).
[16] N. Achiwa, S. Yano, M. Yuzuri, and H. Takaki, J. Phys. Soc. Jpn. **22**, 156 (1967).
[17] K. Yang, K. Kang, Z. Diao, A. Ramanathan, M. H. Karigerasi, D. P. Shoemaker, A. Schleife, and D. G. Cahill, Phys. Rev. Mater. **3**, 124408 (2019).
[18] See Fig. S2 of Supplemental Material at http://link.aps.org/supplemental/10.1103/PhysRevB.102.064415 for the estimate of the misorientation from the twofold component of the torque data; Fig. S1 for field-dependent torque in the Fe_2As (001) plane at temperature $T > 4$ K; Fig. S3 for density-functional-theory calculated magnetic anisotropy; and Fig. S4 for the antiferromagnetic resonance mode.
[19] G. Kresse and J. Furthmüller, Phys. Rev. B **54**, 11169 (1996).
[20] G. Kresse and D. Joubert, Phys. Rev. B **59**, 1758 (1999).
[21] P. E. Blöchl, Phys. Rev. B **50**, 17953 (1994).
[22] H. J. Monkhorst and J. D. Pack, Phys. Rev. B **13**, 5188 (1976).
[23] D. M. Ceperley and B. J. Alder, Phys. Rev. Lett. **45**, 566 (1980).
[24] J. P. Perdew, K. Burke, and M. Ernzerhof, Phys. Rev. Lett. **77**, 3865 (1996).
[25] D. Hobbs, G. Kresse, and J. Hafner, Phys. Rev. B **62**, 11556 (2000).
[26] A. Schrön, C. Rödl, and F. Bechstedt, Phys. Rev. B **86**, 115134 (2012).
[27] T. Nagamiya, K. Yosida, and R. Kubo, Adv. Phys. **4**, 1 (1955).
[28] M. Wang, C. Andrews, S. Reimers, O. J. Amin, P. Wadley, R. P. Campion, S. F. Poole, J. Felton, K. W. Edmonds, B. L. Gallagher, A. W. Rushforth, O. Makarovsky, K. Gas, M. Sawicki, D. Kriegner, J. Zubáč, K. Olejník, V. Novák, T. Jungwirth, M. Shahrokhvand *et al.*, Phys. Rev. B **101**, 094429 (2020).
[29] C. Kittel, *Introduction to Solid State Physics* (Wiley, New York, 1953).
[30] C. Kittel, Phys. Rev. **82**, 565 (1951).
[31] A. B. Shick, S. Khmelevskyi, O. N. Mryasov, J. Wunderlich, and T. Jungwirth, Phys. Rev. B **81**, 212409 (2010).
[32] P. Wadley, S. Reimers, M. J. Grzybowski, C. Andrews, M. Wang, J. S. Chauhan, B. L. Gallagher, R. P. Campion, K. W. Edmonds, S. S. Dhesi, F. Maccherozzi, V. Novak, J. Wunderlich, and T. Jungwirth, Nat. Nanotechnol. **13**, 362 (2018).
[33] T. Matalla-Wagner, M. F. Rath, D. Graulich, J. M. Schmalhorst, G. Reiss, and M. Meinert, Phys. Rev. Appl. **12**, 064003 (2019).